Supplement of Solid Earth, 11, 669–690, 2020
https://doi.org/10.5194/se-11-669-2020-supplement

Solid Earth
Open Access

Supplement of

Seismic waveform tomography of the central and eastern Mediterranean upper mantle

Nienke Blom et al.

Correspondence to: Nienke Blom (nienke.blom@esc.cam.ac.uk)

In this Supplementary material, we report the events used in the inversion (Section S1), the adaptations made to the parameters of certain events (Section S2), the processing applied to raw gradients in the inversion as well as the processing applied to cumulative updates after some sets of iterations (Section S3) and we show extra depth slices of the spike tests from Section 6.3 in the paper. Separate to this document, we provide a video of a 3-D visualisation of the final model, as well as the vtk and ParaView files corresponding to this.

S1 List of events used in the inversion

Table S1 contains all events used in the inversion. Events whose parameters were shifted are included in the table twice: once with the original parameters (from the CMT catalogue, Ekström et al., 2012; Dziewonski et al., 1981, http://www.globalcmt.org) and once with adapted parameters. Original events are marked with a star (*), adapted events are italicised. The final column gives the iterations in which each of the events were used.

The new events that are used to test the final model and which are not used in the inversion are included at the end of the table below a double horizontal line. Letters A–E correspond to the letters A–E in Figure 14 in the manuscript.

	Origin time (UTC)	Latitude [°]	Longitude [°]	Depth [km]	Magnitude [Mwc]	Iterations
event_01	2014-05-24 09:25:18	40.30	25.67	12.0	6.90	0–100
event_03	2000-06-15 21:30:36	34.45	20.49	15.0	5.10	0–19
event_04	2013-06-16 21:39:07	34.22	25.19	20.0	6.10	0–100
event_06	2012-10-19 03:35:14	32.44	31.02	29.0	5.00	0–100
event_07	2010-11-14 23:08:28	36.48	36.08	12.0	4.90	0–100
event_08	2008-02-15 10:36:21	33.27	35.32	12.1	5.10	0–100
event_09	2010-11-03 00:57:00	43.67	20.65	13.8	5.50	0–100
event_12	2000-06-06 02:41:52	40.75	32.70	15.0	6.00	0–100
event_14	2009-12-29 11:08:56	32.56	15.04	12.0	5.00	0–100
event_16	2015-10-09 14:39:19	40.80	36.62	17.8	5.00	0–100
event_19	2012-04-26 22:05:34	39.09	29.25	13.6	4.80	0–100
event_24	2009-05-24 16:17:53	41.17	22.79	12.8	5.30	0–100
event_25	2014-11-07 17:13:01	38.15	22.12	13.2	5.10	0–100
event_29	1998-05-28 18:33:33	31.39	27.36	39.0	5.50	0–19
event_31	2015-04-15 08:25:15	34.72	32.36	17.9	5.30	0–100
event_32	2002-09-06 01:21:33	38.42	13.57	15.0	5.90	0–65
event_33 *	2009-04-06 01:32:49	42.29	13.35	12.0	6.30	0–28
event_33_shift	***2009-04-06 01:32:46***	*42.29*	*13.35*	*12.0*	*6.30*	*30–100*
event_34	2008-02-14 10:09:29	36.24	21.79	20.0	6.80	0–100
event_35	2009-09-06 21:49:46	41.37	20.36	12.0	5.50	0–100
event_36	2013-10-12 13:11:56	35.37	23.37	15.0	6.80	0–100
event_37	2015-11-17 07:10:12	38.47	20.53	15.0	6.50	0–100
event_38 *	2012-06-10 12:44:19	36.28	29.06	28.4	6.10	0–65
event_38_shift	*2012-06-10 12:44:19*	***36.34***	***29.00***	*28.4*	*6.10*	*65–100*
event_39	2002-02-03 07:11:43	38.62	31.21	15.0	6.50	0–19
event_40	2010-03-08 02:32:37	38.82	40.04	15.1	6.10	0–100
event_41	2015-06-27 15:34:03	28.83	34.62	28.3	5.60	0–100
event_42	2012-05-22 00:00:33	42.51	23.05	12.8	5.60	0–100

Continued on next page

	Origin time (UTC)	Latitude [°]	Longitude [°]	Depth [km]	Magnitude [Mwc]	Iterations
event_43	2002-11-01 15:09:09	41.80	14.88	15.0	5.70	0–85
event_44	2003-03-29 17:42:21	42.89	15.22	15.0	5.50	0–85
event_45	2004-02-11 08:15:06	31.62	35.31	26.1	5.30	0–100
event_46	2012-05-11 18:48:32	34.22	34.17	25.5	5.30	0–100
event_47	2001-06-25 13:28:52	37.23	35.71	15.0	5.40	0–19
event_48	2008-11-12 14:03:21	38.92	35.46	17.0	5.10	0–100
event_49	2003-07-13 01:48:25	38.16	38.90	15.0	5.50	0–85
event_50	2002-06-24 01:20:42	36.03	10.29	15.0	5.20	0–65
event_51	2011-07-07 19:21:50	41.94	7.63	13.3	5.10	0–100
event_53	2010-11-03 18:13:13	39.95	12.89	491.8	5.20	0–19
event_54	2012-05-20 02:03:56	44.89	11.44	12.0	6.10	0–65
event_55	2009-08-05 07:49:04	43.42	28.60	19.9	5.00	0–100
event_56	2012-03-26 10:35:35	39.15	42.20	19.5	5.20	0–100
event_57	2007-01-21 07:39:01	39.60	42.72	14.7	5.10	0–100
event_58	2012-10-25 23:05:28	39.88	15.98	12.0	5.30	0–100
event_59	2009-11-03 05:25:13	37.35	20.19	15.5	5.80	0–100
event_61	2007-08-31 20:52:45	36.59	26.32	15.7	5.20	0–100
event_62	2016-08-24 02:33:32	42.68	13.15	12.0	5.60	0–100
event_63	2007-11-09 01:43:09	38.78	25.66	15.2	5.18	0–100
event_64	2008-08-03 00:39:19	39.54	23.76	12.0	5.25	0–100
event_65	2005-10-17 05:45:24	38.21	26.59	15.2	5.48	0–100
event_66	2013-01-08 14:16:11	39.62	25.61	14.6	5.81	0–100
event_67	2009-08-21 13:40:01	41.76	19.07	21.1	5.06	0–100
event_68	2013-07-21 01:32:27	43.48	13.68	12.0	5.11	0–100
event_69	2006-05-25 23:14:41	36.55	19.91	23.5	5.19	0–100
event_70	2007-02-03 13:43:25	35.67	22.39	53.5	5.40	0–100
event_71	2008-06-12 00:20:49	35.28	26.36	40.7	5.13	0–100
event_72	2011-05-19 20:39:05	34.32	23.66	17.8	5.24	0–100
event_73	2012-01-27 01:33:25	35.89	24.88	15.6	5.42	0–100
event_74	2005-01-11 04:35:57	36.84	27.84	12.2	5.03	0–19
event_75	2007-05-21 16:39:11	35.14	27.62	18.1	5.03	0–100
event_76	2007-12-20 09:48:32	39.43	33.10	12.0	5.66	0–100
event_77	2011-09-22 03:22:38	39.68	38.60	16.1	5.56	0–85
event_78	2005-06-06 07:41:33	39.44	40.87	15.4	5.64	0–85
event_79	2007-10-29 09:23:19	36.89	29.21	12.0	5.30	0–100
event_80	2015-11-29 00:28:11	38.82	37.75	20.2	5.11	0–100
event_81	2014-08-24 19:43:39	37.64	30.61	18.1	5.09	0–100
event_82	2011-07-25 17:57:22	40.80	27.72	12.0	5.09	0–100
event_83	2012-09-19 09:17:48	37.28	37.12	21.4	5.04	0–100
event_84	2006-10-24 14:00:23	40.46	28.98	14.3	5.05	0–100
event_85	2008-01-06 05:14:23	36.98	22.87	92.4	6.17	0–100
event_86	2014-08-29 03:45:08	36.46	23.62	100.2	5.81	0–100
event_87	2014-04-04 20:08:08	37.11	23.69	122.4	5.59	0–100
event_88	2008-06-18 01:58:45	37.63	22.78	92.5	5.06	0–100
event_89	2007-10-27 05:29:43	37.70	21.33	27.5	5.11	0–100
event_90	2006-10-26 14:28:39	38.65	15.41	216.8	5.79	0–100
event_91	2005-07-10 13:10:15	42.37	19.70	12.0	5.15	0–100
event_92	2005-09-27 00:25:39	43.18	18.18	29.9	5.09	0–100
event_93	2013-06-21 10:34:00	44.10	10.17	12.0	5.32	0–100
event_94	2015-06-09 01:09:06	38.51	23.43	12.6	5.28	0–100
event_95	2007-04-10 10:41:05	38.55	21.48	12.0	5.16	0–85
event_96	2013-07-02 10:45:23	39.97	21.74	28.0	5.06	0–100
event_97	2007-06-29 18:09:15	39.19	20.11	12.0	5.43	0–100
event_98 *	2013-12-28 15:21:06	35.82	30.97	52.6	5.93	0–65
event_98_shift	*2013-12-28 15:21:06*	***35.97***	***31.22***	*52.6*	*5.93*	*65–100*
event_99	2012-07-09 13:55:00	35.36	28.96	71.2	5.74	0–100
event_100	2016-10-30 06:40:24	42.75	13.16	12.0	6.60	10–100
event_101*	2016-08-24 01:36:36	42.64	13.22	12.0	6.20	10–65

Continued on next page

	Origin time (UTC)	Latitude [°]	Longitude [°]	Depth [km]	Magnitude [Mwc]	Iterations
event_101_shift	***2016-08-24 01:36:37***	*42.64*	*13.22*	*12.0*	*6.20*	*65–100*
event_102 (D)	2017-07-20 22:31:17	36.80	27.62	12.0	6.60	
event_104 (C)	2017-06-12 12:28:41	38.81	26.32	12.0	6.40	
event_105	2017-03-02 11:07:27	37.53	38.45	17.2	5.60	
event_106 (B)	2018-01-04 10:46:12	42.60	19.82	14.7	5.20	
event_107 (A)	2017-01-18 10:14:14	42.48	13.28	12.0	5.70	
event_109 (E)	2016-05-16 01:45:59	28.45	34.58	15.0	5.30	

Table S1: Overview of all events used in the inversion (events 1–101) and used for validation (events 102–109). Numbering is discontinuous because some events have been discarded after initial data inspection e.g. due to a poor signal-to-noise ratio, or limited data availability.

S2 Adapted event parameters

Below, we discuss the changes that were made to certain event parameters, including the rationale behind these changes. The actual parameters are given in Table S1 above.

Event 33

In practically all seismograms, a static shift between observed and synthetic traces is observed (Figure S1). This is independent from epicentral distance and is visible on all components. It is confirmed by the spatial distribution of phase shifts, and the skewed histogram of phase shifts as demonstrated in Figure S2. A time shift of 3 seconds was applied to remove this static shift. As a result, the phase shifts centre around a roughly zero mean (Figure S3).

A time shift is not the only way in which the shift can be explained; however, for the purposes of the inversion (and given the additional constraints given by other events in the area) it is the easiest and most workable explanation.

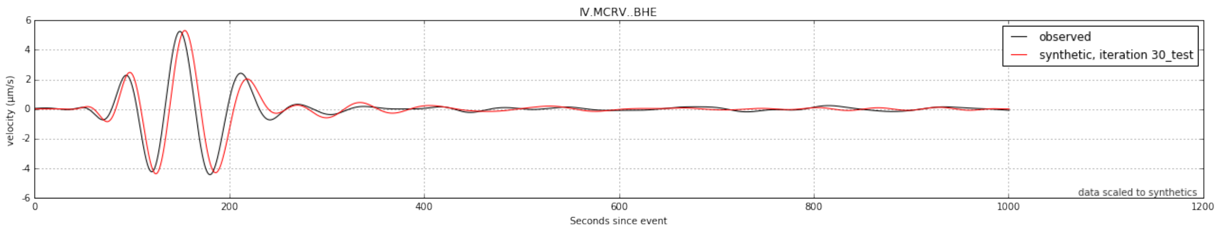

(a) Station IV.MCRV (E component).

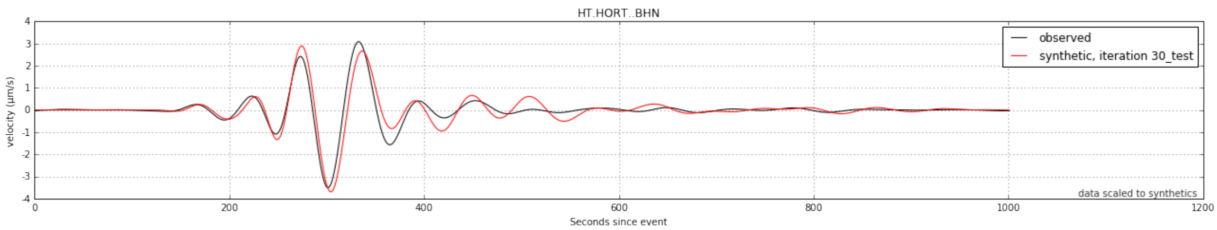

(b) Station HT.HORT (N component).

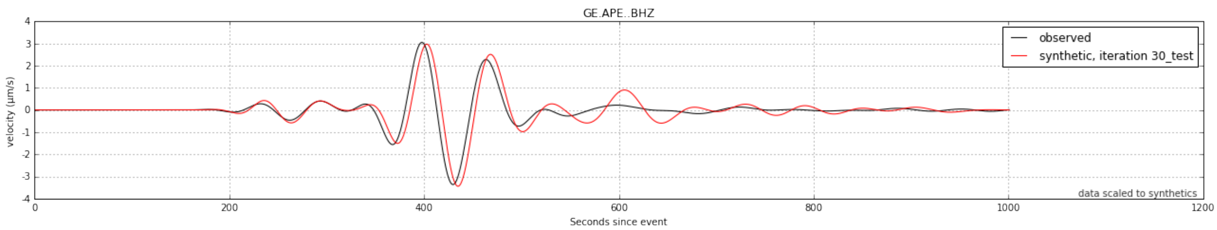

(c) Station GE.APE (Z component).

Figure S1: Seismograms for event 33 (uncorrected) and iteration 30 (55–150 s).

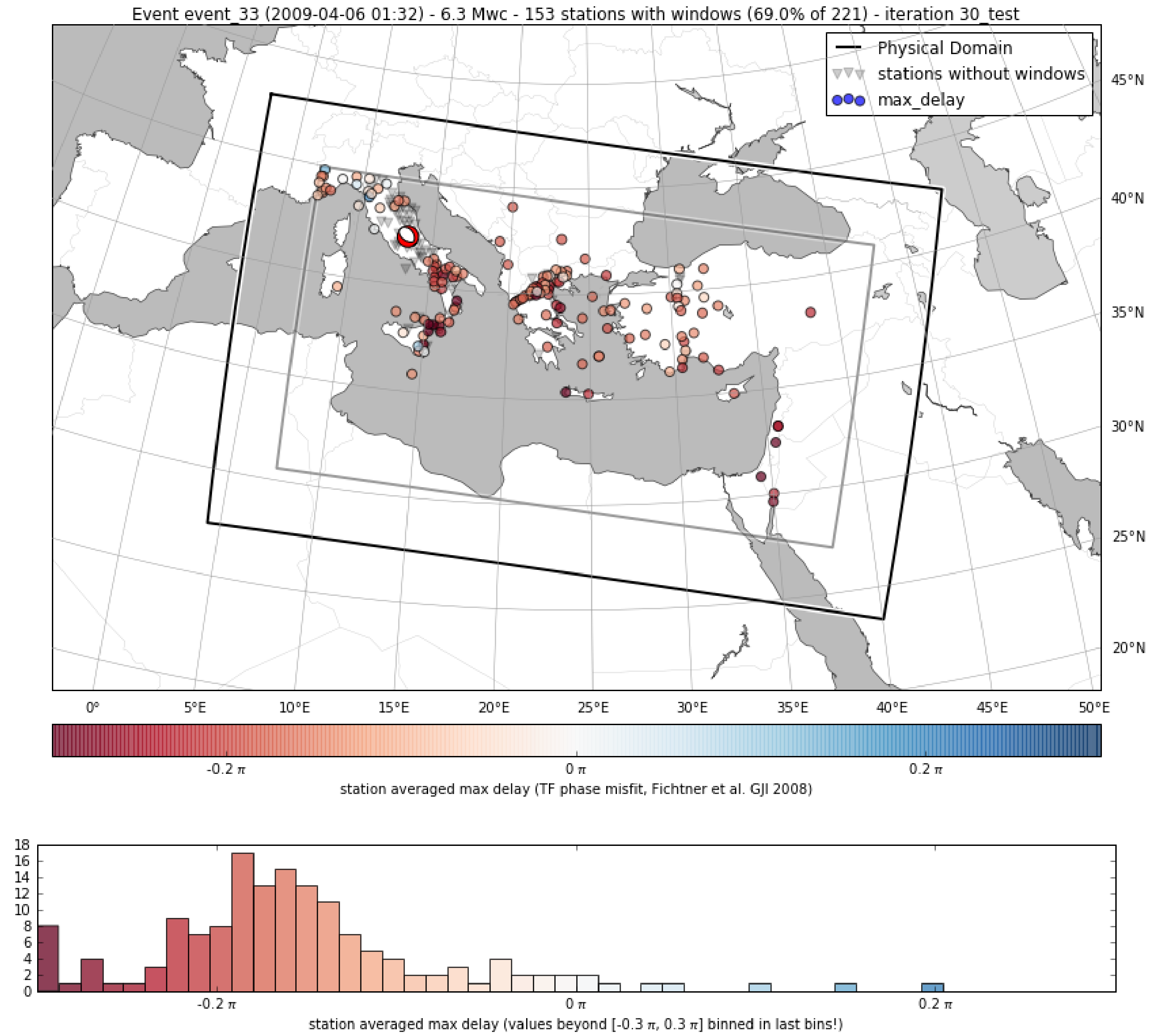

Figure S2: Original distribution of "max delay" phase shifts for event 33 at iteration 30 (55–150 s). This value is computed for each window as $\max(W_p\,(\phi - \phi_{\mathrm{obs.}}))$ – see Equation 2 in the manuscript.

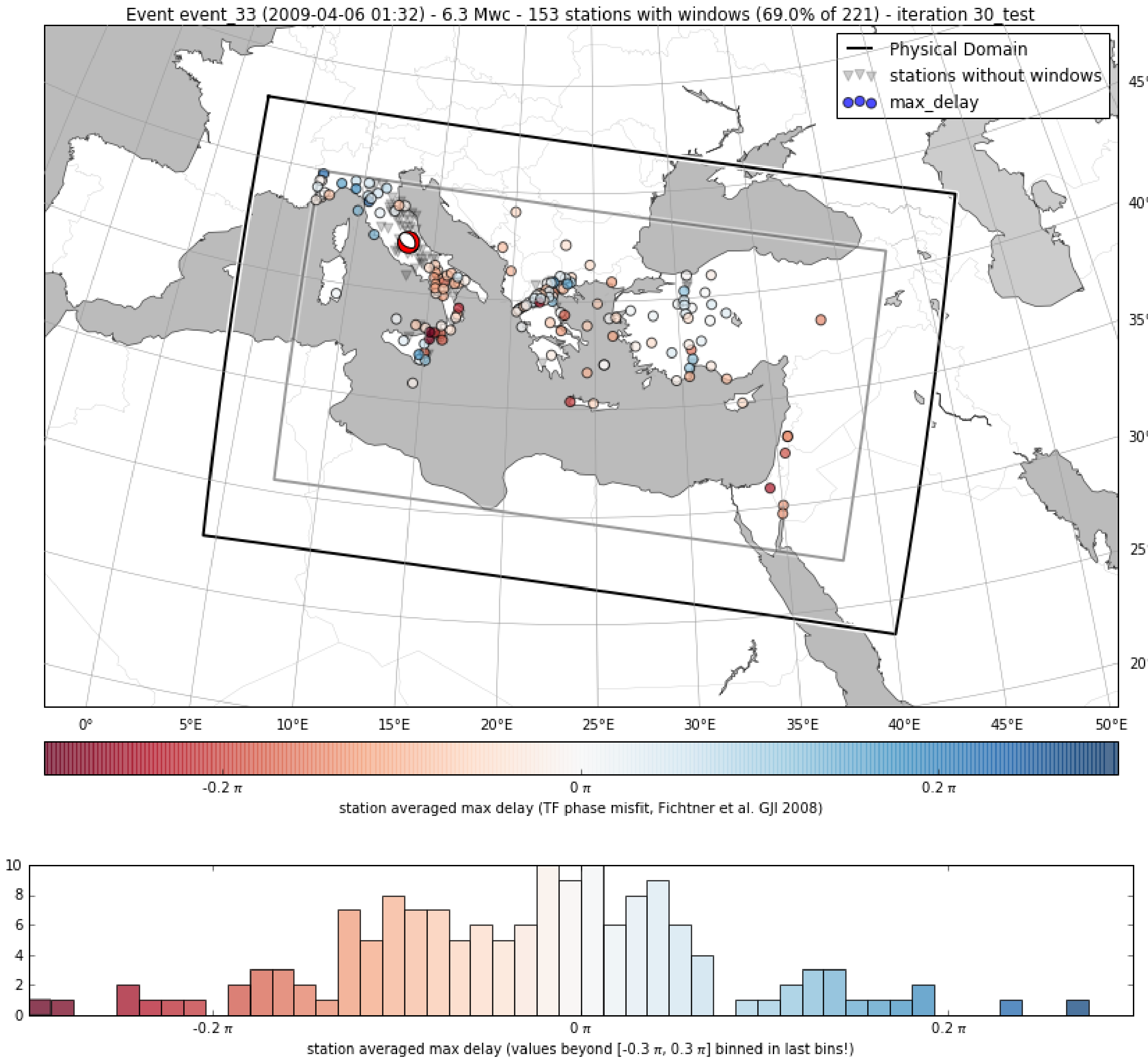

Figure S3: Distribution of "max delay" phase shifts for event 33 at iteration 30 (55–150 s) after shifting the event origin time by 3 seconds forward.

Event 38

Event 38 shows a geographical pattern of phase shifts, with positive shifts towards the north-west and negative shifts towards the south-east (Figure S4). Such phase shifts were not encountered for other events in the same area. This geographical pattern is therefore most easily explained using a small shift of the event towards the north-west. As a result of the applied shift in location, the spatial pattern of space shifts didappears and the histogram of phase shifts centres more around zero (Figure S5). The new location also corresponds more closely with the reported ISC-EHB location (Engdahl et al., 1998; Weston et al., 2018).

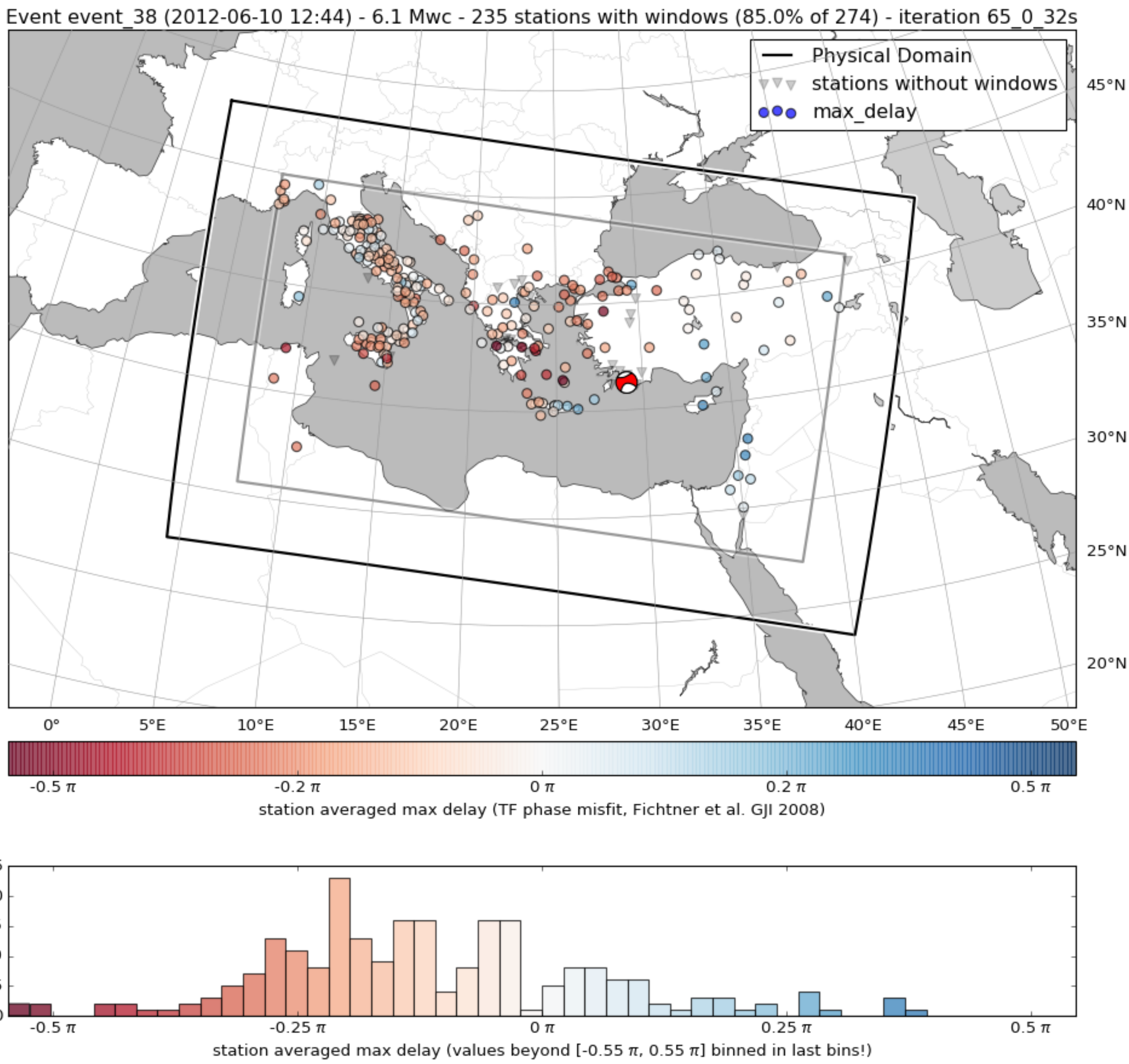

Figure S4: Original distribution of “max delay” phase shifts for event 38 at iteration 65 (32–150 s).

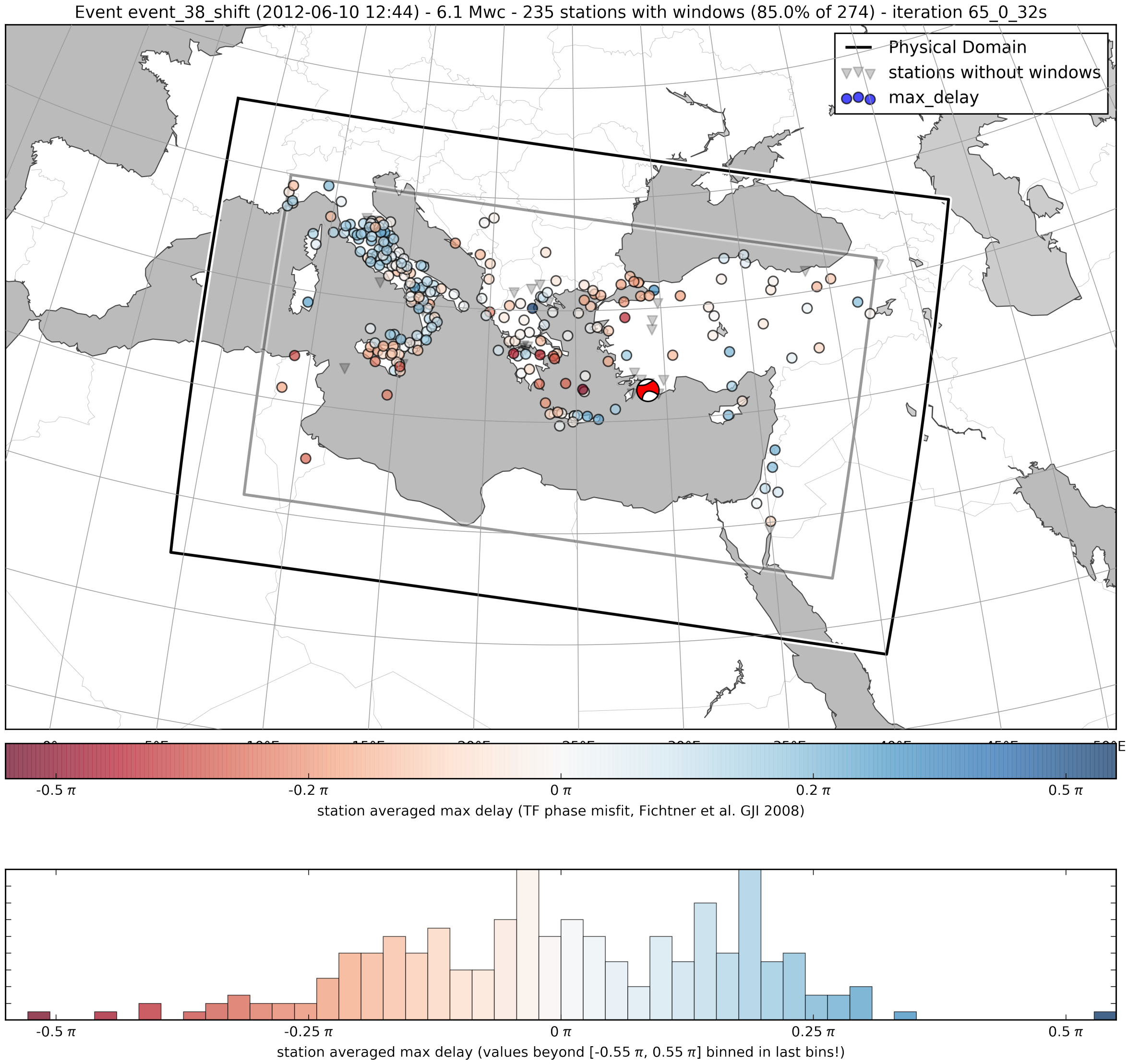

Figure S5: Distribution of “max delay” phase shifts for event 38 at iteration 65 (32–150 s) after shifting the event location towards the north-east (latitude + 0.06°, longitude - 0.06°).

Event 98

Event 98 shows a strong geographical pattern of phase shifts, with positive shifts towards the south-west and negative shifts towards the north-east (Figure S6). Such phase shifts were not encountered for other events in the same area. This geographical pattern is therefore most easily explained using a relocation of the event towards the north-east. As a result of this, the spatial pattern disappears entirely and the histogram becomes more unimodal and centering around zero (Figure S7). The new location also corresponds more closely with the reported ISC-EHB location (Engdahl et al., 1998; Weston et al., 2018).

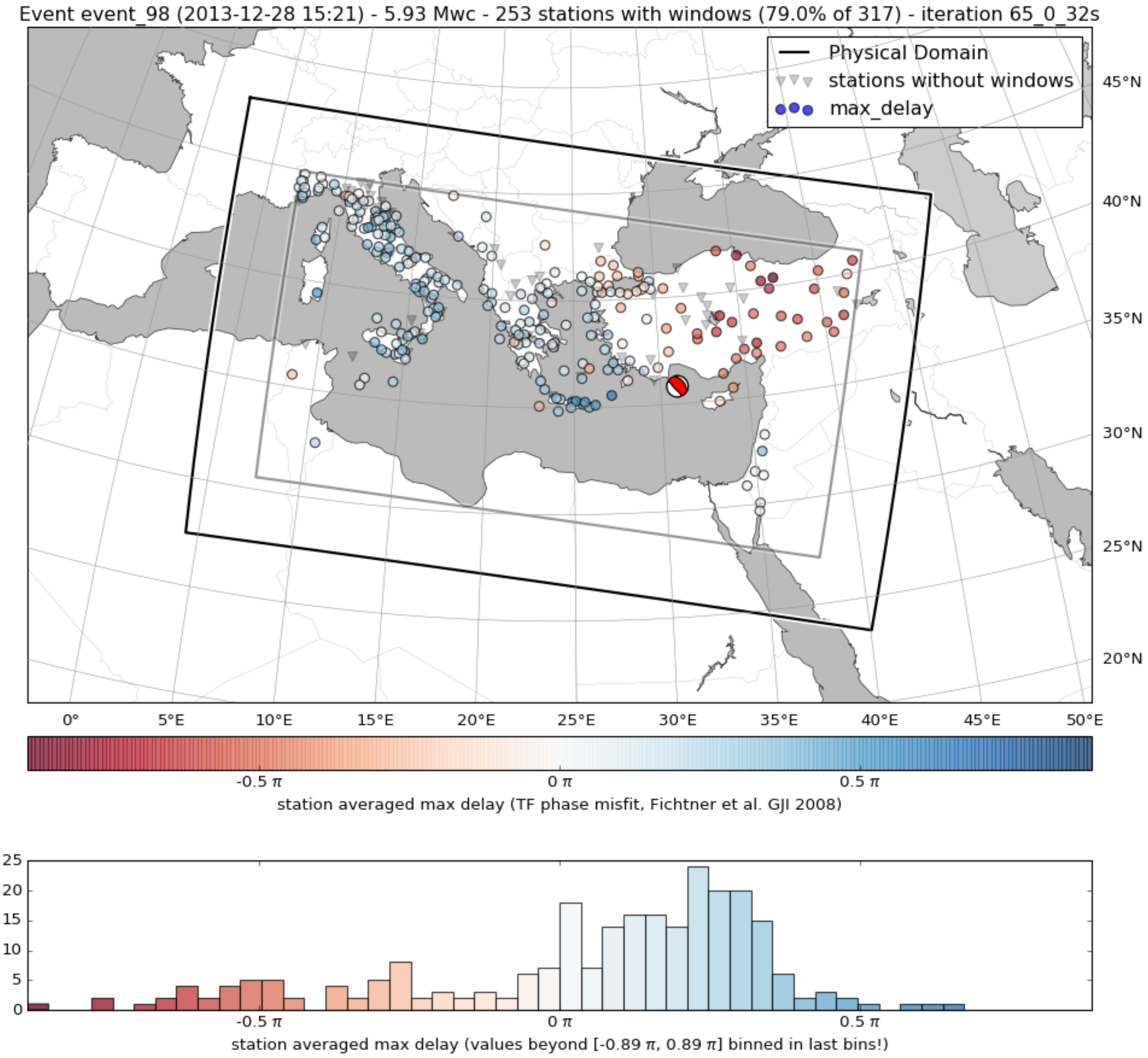

Figure S6: Original distribution of "max delay" phase shifts for event 98 at iteration 65 (32–150 s).

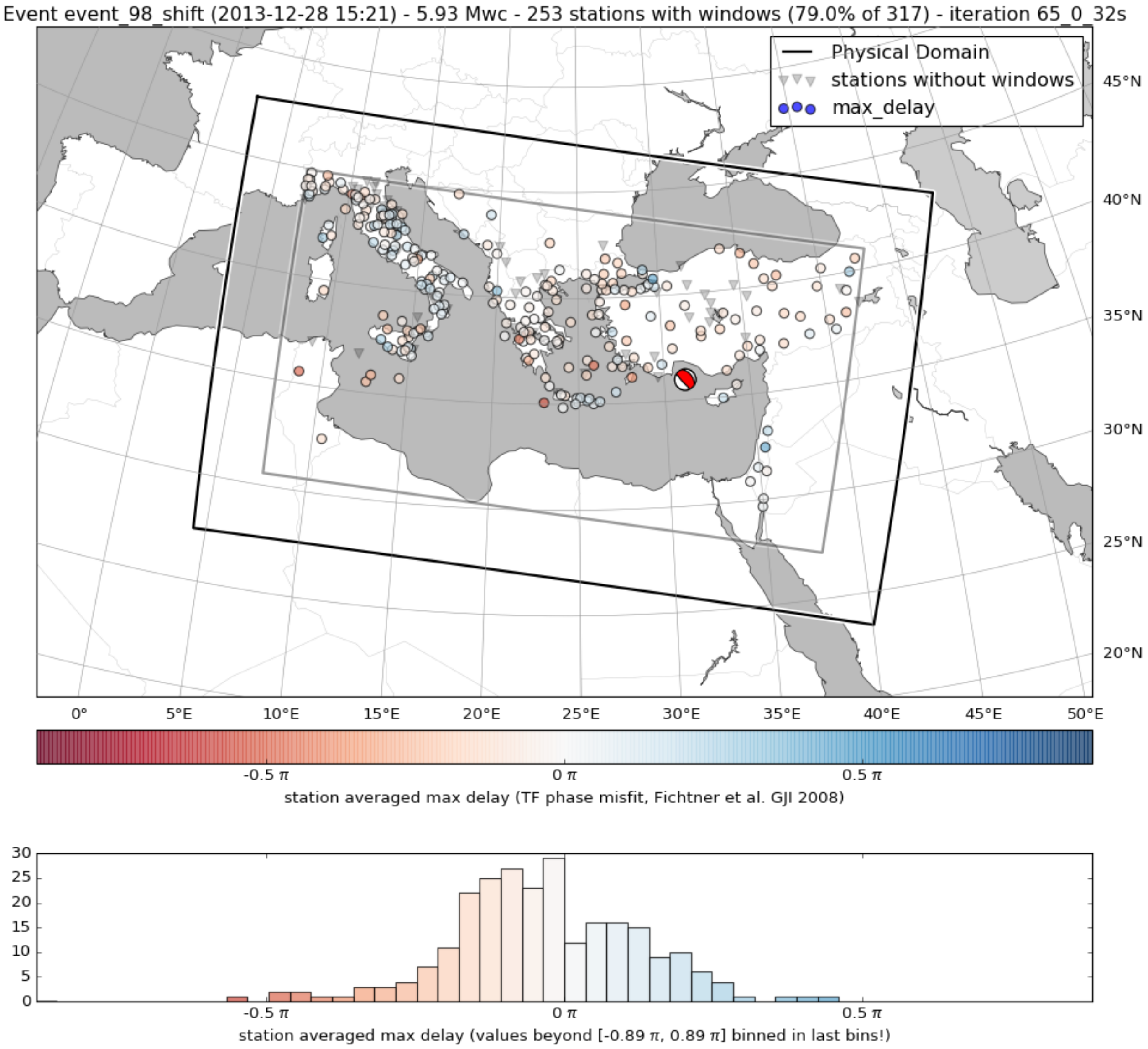

Figure S7: Distribution of "max delay" phase shifts for event 98 at iteration 65 (32–150 s) after shifting the event location towards the north-east (latitude + 0.15°, longitude + 0.25°).

Event 101

Event 101 fairly consistently showed synthetic waveforms arriving ahead of their corresponding observed data waveforms (Figure S8). This is confirmed by the spatial distribution and histogram of phase shifts, as demonstrated in Figure S9, where the histogram is skewed towards positive phase shifts (i.e. synthetics ahead of observed data). A time shift of 1 second was applied to remove this static shift. As a result, the spatial pattern of phase shifts centred around zero (Figure S3).

As with event 33, a time shift is not the only way in which the shift can be explained; however, for the purposes of the inversion (and given the additional constraints given by other events in the area) it is the easiest and most workable explanation.

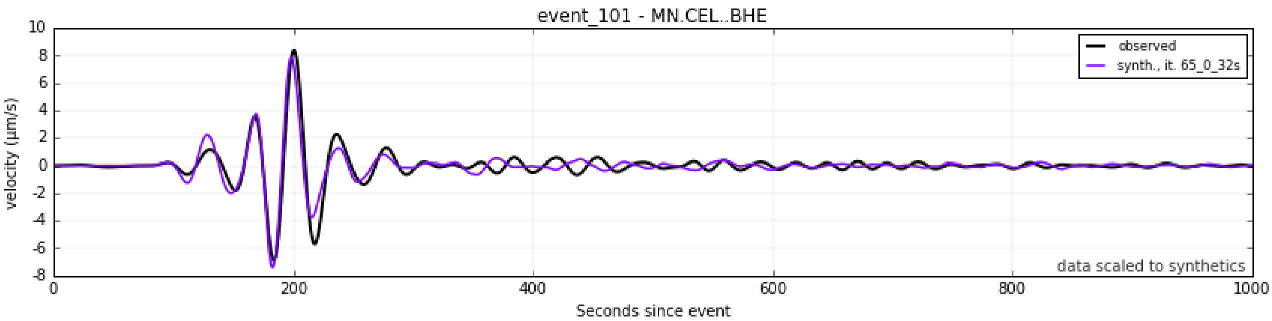

(a) Station MN.CEL (E component).

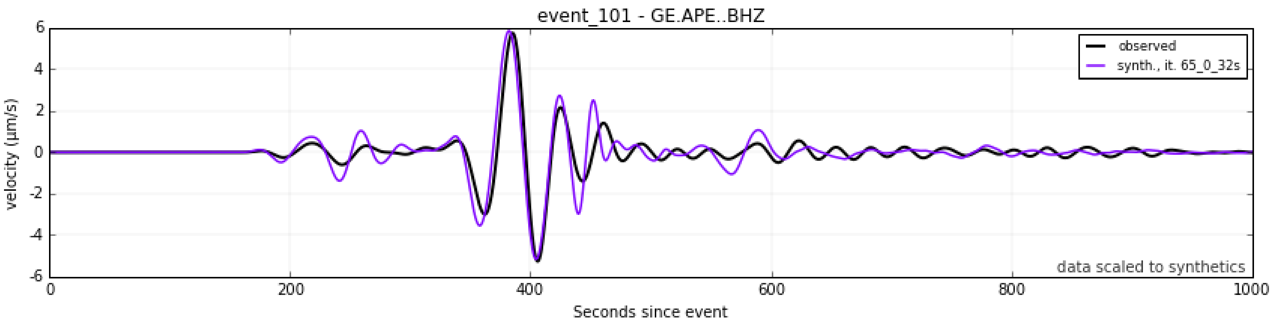

(b) Station GE.APE (Z component).

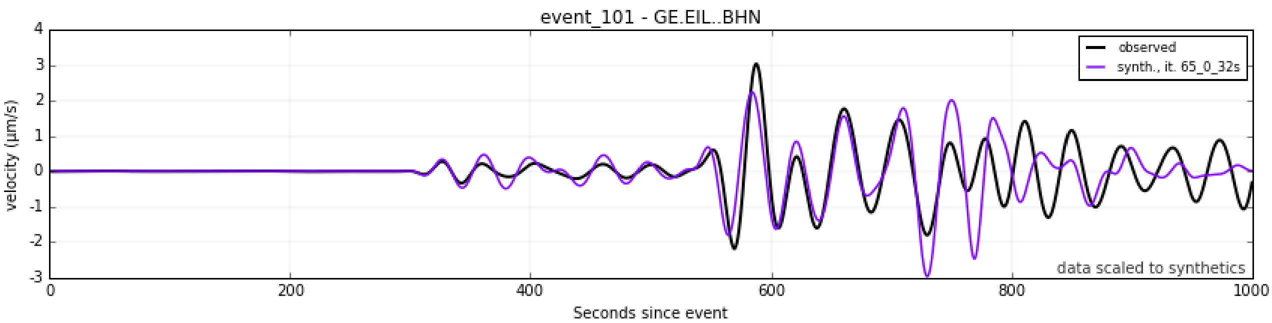

(c) Station GE.EIL (N component).

Figure S8: Seismograms for event 101 (uncorrected) and iteration 65_0_32s (32–150 s).

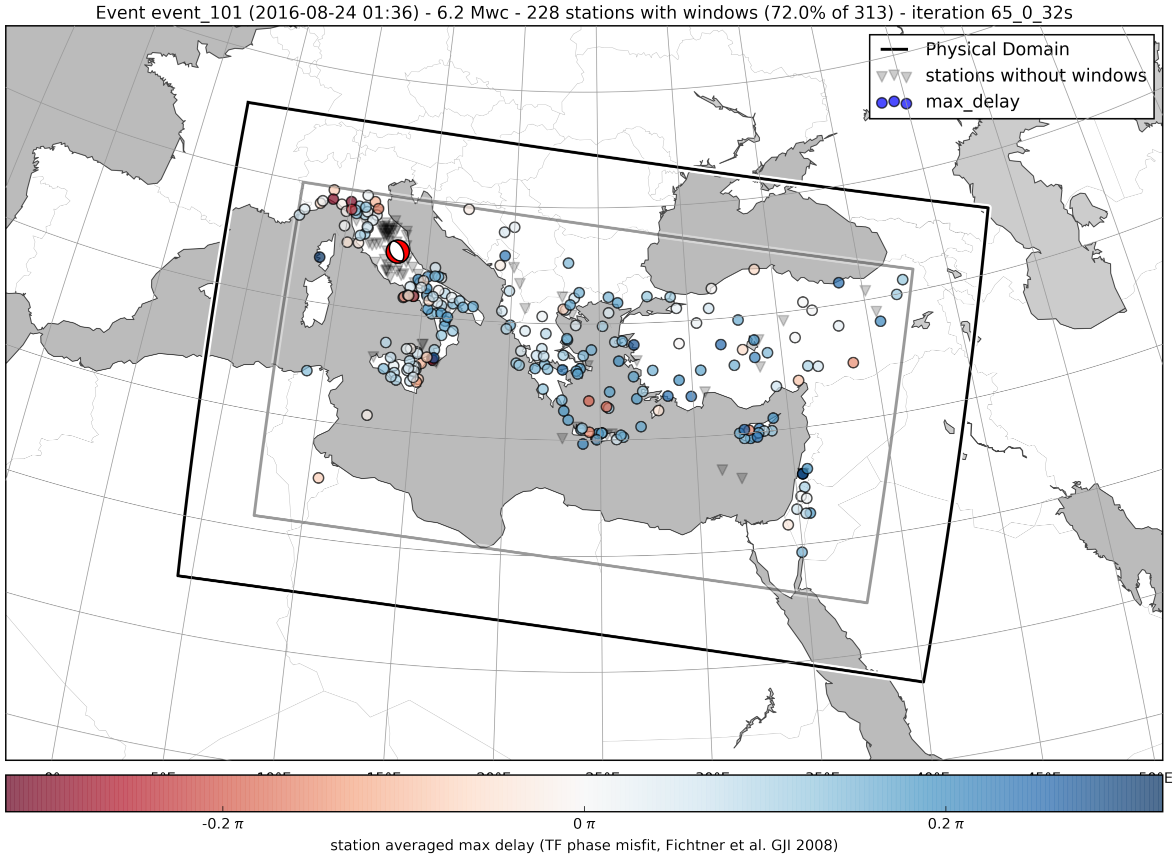

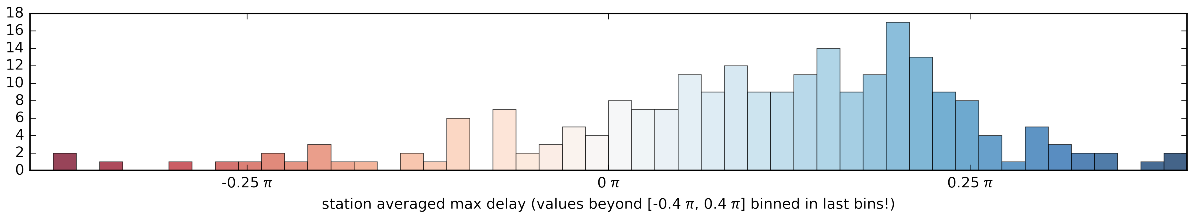

Figure S9: Original distribution of "max delay" phase shifts for event 101 at iteration 65_0_32s (32–150 s). This value is computed for each window as $\max(W_p\,(\phi - \phi_{\mathrm{obs.}}))$ – see Equation 2 in the manuscript.

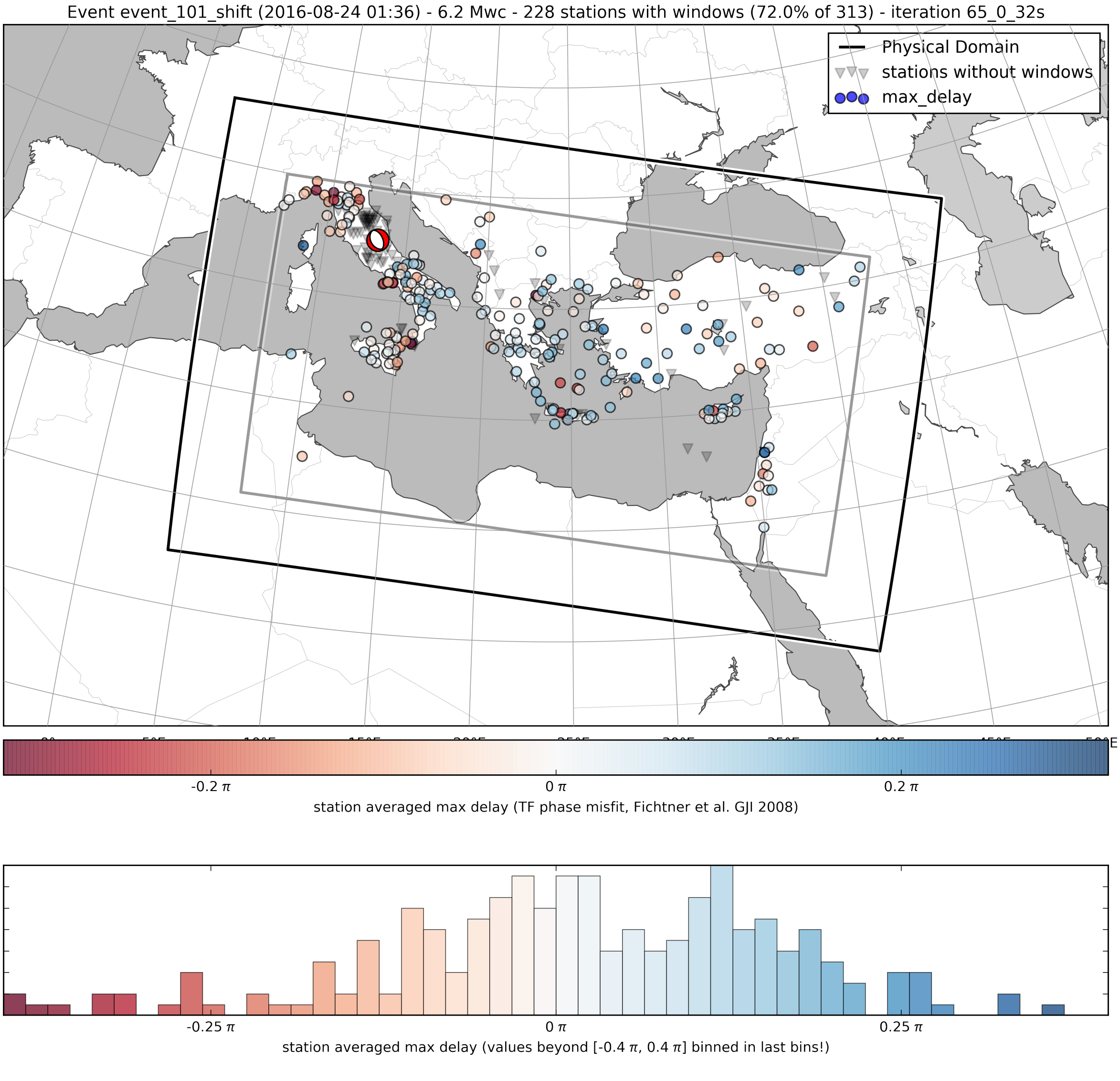

Figure S10: Distribution of "max delay" phase shifts for event 101 at iteration 65_0_32s (32–150 s) after shifting the event origin time by 1 second forward.

S3 Processing of model updates

In order to compute a model update, the raw gradients for each model parameter are preprocessed before a descent direction is computed. This is done in order to improve convergence properties of the gradients. Kernels for each event are clipped at the 99th percentile in order to avoid too-strong localisation of updates especially in the source region, and then summed to produce the misfit gradient. The side and bottom edges are set to zero to remove potential boundary effects, and some smoothing is applied. This processing routine is based on experience from previous inversions and some initial experimentation, and the chosen parameters, re-evaluated for every set of iterations, are given in Table S2.

Additionally, at the end of certain sets of iterations, the cumulative model update is processed. These processing parameters are given in italics as the "Post-run" values in Table S2.

#	Period range	Frequency band	Number of iterations	Simulation length	Processing
0	100–150 s	0.0067–0.01 Hz	10	1200 s	cut 3°, 100 km; n_{sm}^{hv}=10
					Post-run: cut 4.5°, 350 km; n_{sm}^{h}=10, n_{sm}^{v}=50
1	80–150 s	0.0067–0.0125 Hz	10	1200 s	cut 3°, 100 km; n_{sm}^{hv}=10
					Post-run: cut 4.5°, 370 km; n_{sm}^{h}=3, n_{sm}^{v}=5
2	65–150 s	0.0067–0.0154 Hz	10	1200 s	cut 4.5°, 370 km; n_{sm}^{hv}=10
3	55–150 s	0.0067–0.0182 Hz	10	1001 s	cut 3°, 100 km; n_{sm}^{hv}=10
					Post-run: cut 2.5°, 320 km; n_{sm}^{h}=1, n_{sm}^{v}=3
4	46–150 s	0.0067–0.0217 Hz	10	990 s	cut 2°, 300 km; n_{sm}^{hv}=8
5	38–150 s	0.0067–0.0263 Hz	10	990 s	cut 2°, 300 km; n_{sm}^{hv}=8
					Post-run: density only: n_{sm}^{h}=10, n_{sm}^{v}=35
	38–150 s	0.0067–0.0263 Hz	5	990 s	cut 2°, 300 km; n_{sm}^{h}=3, n_{sm}^{v}=15
					density: n_{sm}^{h}=7, n_{sm}^{v}=60
6	32–150 s	0.0067–0.0313 Hz	15	1000 s	cut 2°, 300 km; n_{sm}^{h}=3, n_{sm}^{v}=15
					density: n_{sm}^{h}=7, n_{sm}^{v}=60
	32–150 s	0.0067–0.0313 Hz	5	1000 s	cut 2°, 300 km; n_{sm}^{h}=2, n_{sm}^{v}=10
					density: n_{sm}^{h}=4, n_{sm}^{v}=20
7	28–150 s	0.0067–0.0357 Hz	15	900 s	cut 2°, 300 km; n_{sm}^{h}=2, n_{sm}^{v}=10
					density: n_{sm}^{h}=4, n_{sm}^{v}=20

Table S2: Overview of inversion choices. The column 'Simulation length' shows the duration of each synthetic earthquake simulation. As frequency increases, the surface wave train becomes more compact (see Figure 3 in the manuscript), so the simulation duration can be shortened. The column 'Processing' indicates the processing applied to the gradients. 'Cut' indicates over which distance the model update is set to zero at the sides (in degrees) or the bottom (in km). This is in order to remove boundary reflection issues. 'n_{sm}' indicates the number of smoothing iterations applied, where superscripts h, v and hv indicate whether this is done in the horizontal direction, in the vertical direction, or simultaneously in the horizontal and vertical directions. In some iterations, additional smoothing was carried out to compensate for smoothing set to values that turned out to be too low. This is indicated in italics. After the first five period bands, separate smoothing for density is introduced, in order to avoid the accumulation of unphysical density values.

S4 Additional depth slices

In Figure S11 we show additional depth slices for our final model, as an extension of Figure 10 of the paper. The deeper we go, the less pronounced the anomalies are.

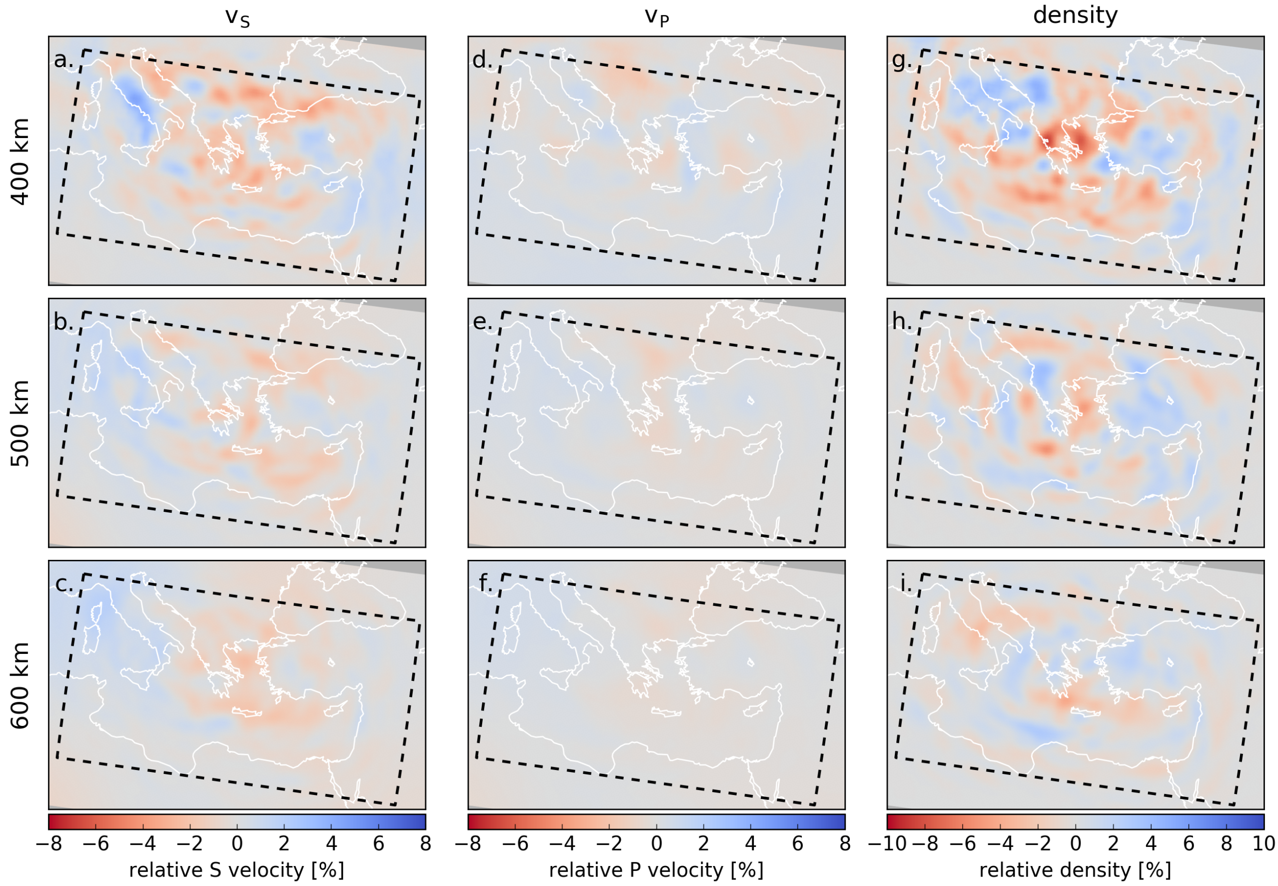

Figure S11: Addional depth slices for the final model, at depths of 400, 500 and 600 km.

S5 Comparison with model UU-P07

In Figures S12 and S13 we compare our final model with model UU-P07, a globally-derived travel-time P-velocity model (Amaru, 2007). The cross-sections for the latter were obtained using the SubMachine engine (Hosseini et al., 2018). Because the latter model is a P-wave travel-time tomography, the anomalies are of significantly reduced amplitude. For these plots, the colour scale varies from -1 to +1%, as opposed to -8 to +8%.

These figures are essentially an extension of Figures 12 and 13 in the paper. In general, a very good correspondence can be observed between the two models, which is encouraging given that we compare such different datasets, parameters and modelling methods.

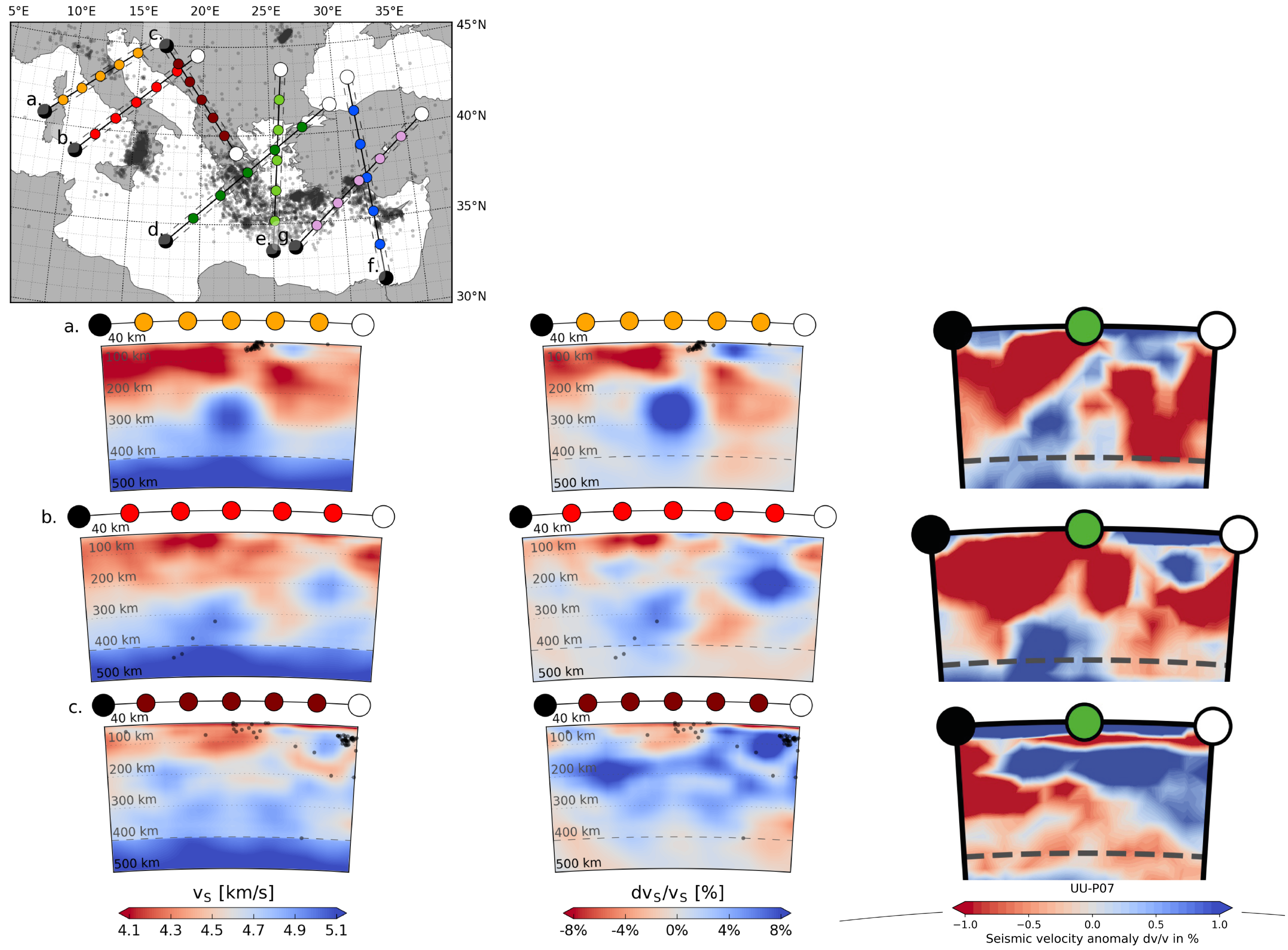

Figure S12: A comparison between our final model and model UU-P07 (Amaru, 2007). Note the different colour scales for the different models.

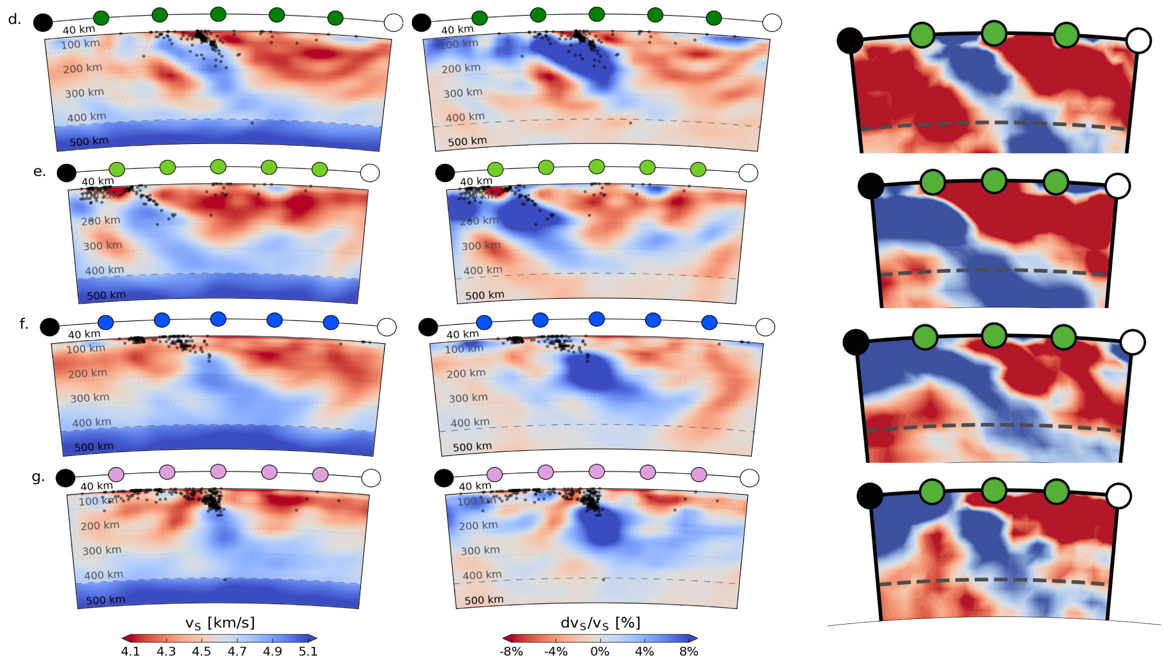

Figure S13: Continuation of the model comparison of Figure S12.

S6 Spike tests: additional depth slices

As described in Section 6.3 of the paper, we execute spike tests to assess recovery and trade-offs between the parameters. Figure 15 in the paper shows the result of this at a depth of 100 km. Here, we show depth slices at depths of 50, 300 and 500 km as well as repeating the slice at 100 km for reference (Figures S6–S6). As the depth increases, less of the input anomalies is recovered, and smearing is greater. Recovery of v_{SH} is most significant at depth. As this is the band with shortest periods, the updates are strongest at depths of <300 km.

It is also worth noticing that the slice at 50 km depth shows a strong trade-off between parameters, as well as some 'overcompensation' of the opposite sign in between the spikes. This further demonstrates that in the currently considered period band, results at these depths should not be interpreted.

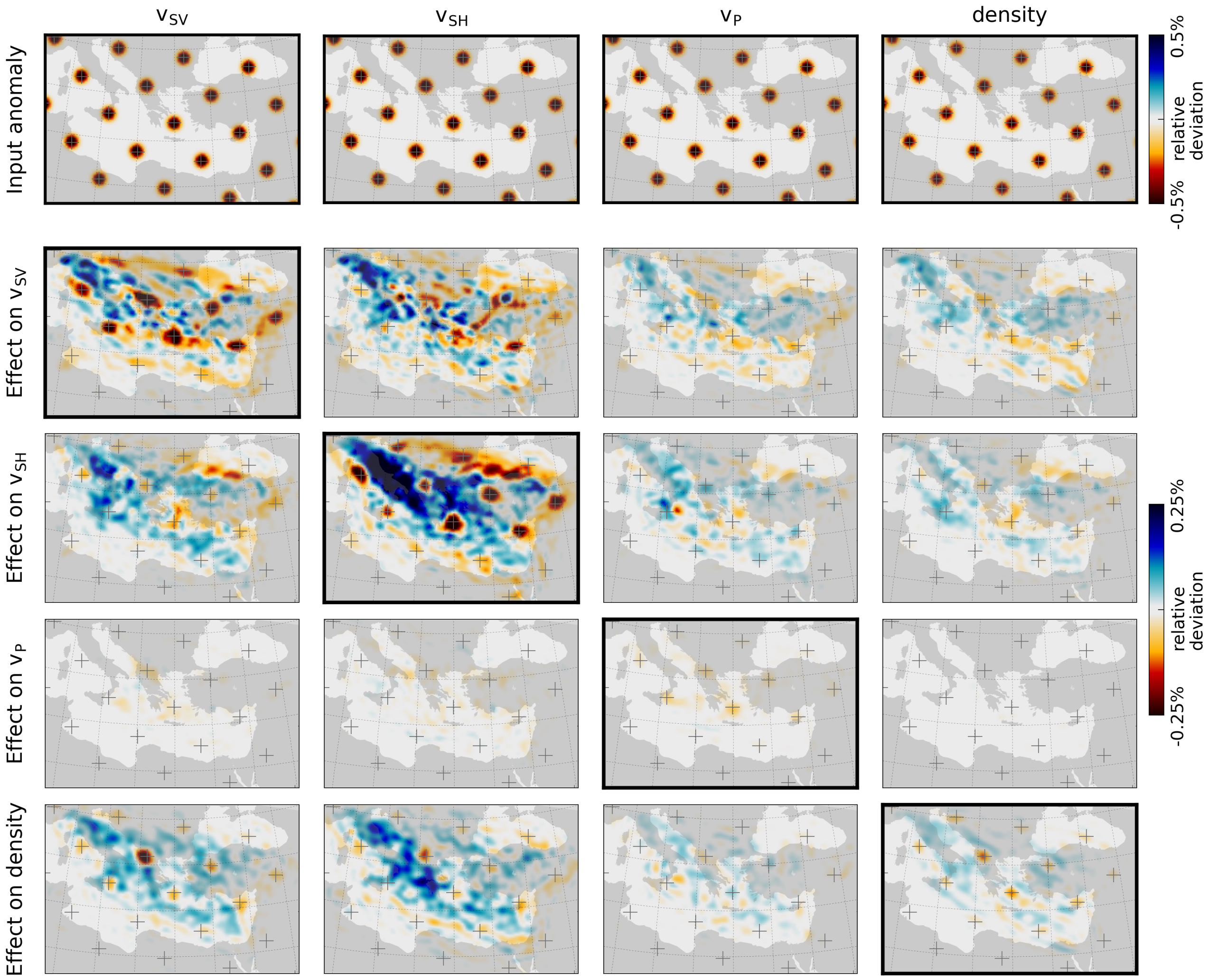

Figure S14: Spike tests conducted for model 91 in the period band 28–150 s, as described in Figure 15 of the paper. Results are here shown for a depth of 50 km.

References

Amaru, M. (2007). *Global travel time tomography with 3-D reference models.* PhD thesis, Utrecht University.

Dziewonski, A. M., Chou, T.-A., and Woodhouse, J. H. (1981). Determination of earthquake source parameters from waveform data for studies of global and regional seismicity. *Journal of Geophysical Research: Solid Earth*, 86(B4):2825–2852.

Ekström, G., Nettles, M., and Dziewonski, A. M. (2012). The global CMT project 2004-2010: centroid moment tensors for 13,017 earthquakes. *Phys. Earth Planet. Inter.*, 200-201:1–9.

Engdahl, E. R., van der Hilst, R., and Buland, R. (1998). Global teleseismic earthquake relocation with improved travel times and procedures for depth determination. *Bulletin of the Seismological Society of America*, 88(3):722–743.

Hosseini, K., Matthews, K. J., Sigloch, K., Shephard, G. E., Domeier, M., and Tsekhmistrenko, M. (2018). Submachine: Web-based tools for exploring seismic tomography and other models of Earth's deep interior. *Geochemistry, Geophysics, Geosystems*, 19(5):1464–1483.

Weston, J., Engdahl, E. R., Harris, J., DiGiacomo, D., and Storchak, D. A. (2018). ISC-EHB: reconstruction of a robust earthquake data set. *Geophysical Journal International*, 214(1):474–484.

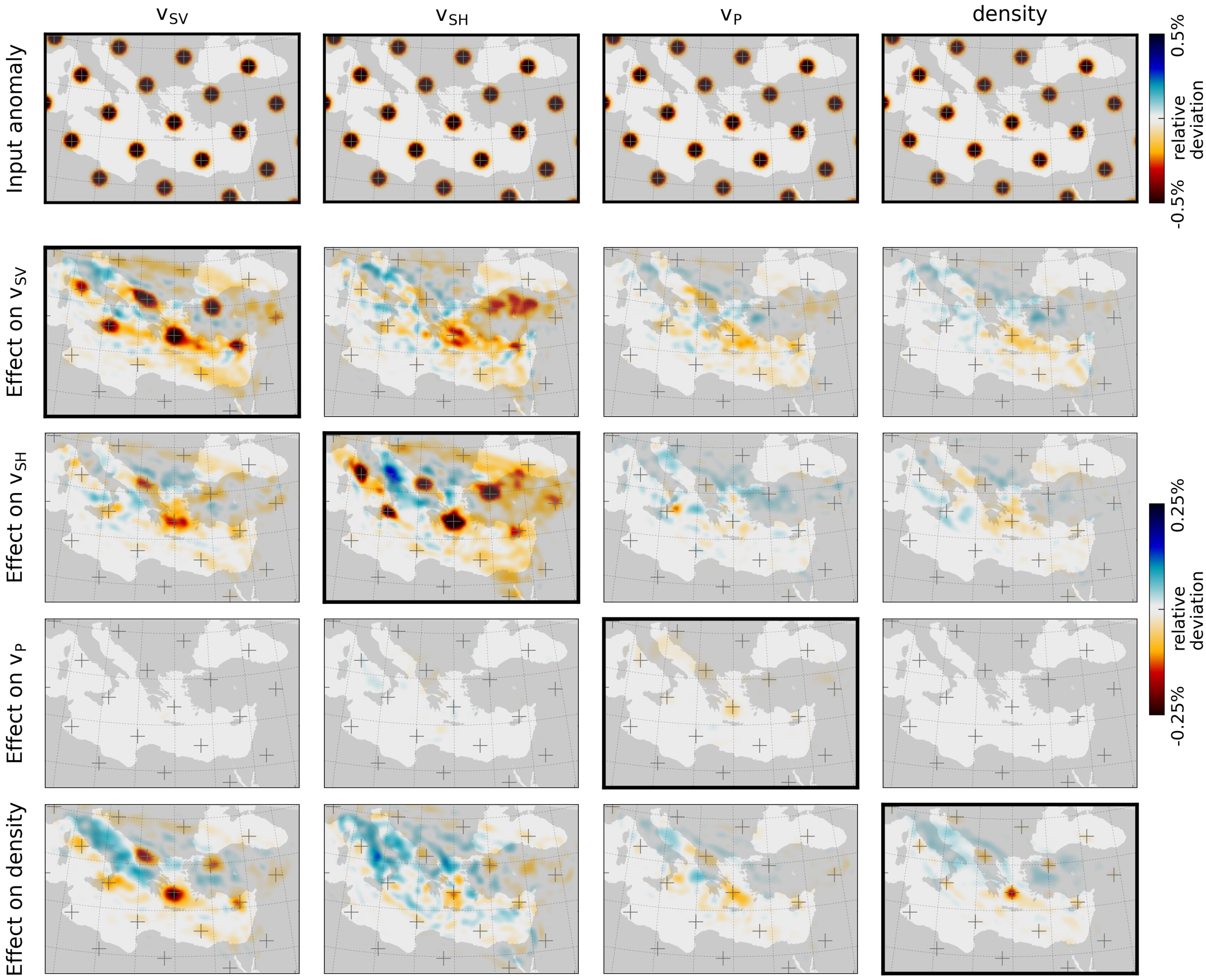

Figure S15: Spike tests conducted for model 91 in the period band 28–150 s, as described in Figure 15 of the paper. Results are here shown for a depth of 100 km.

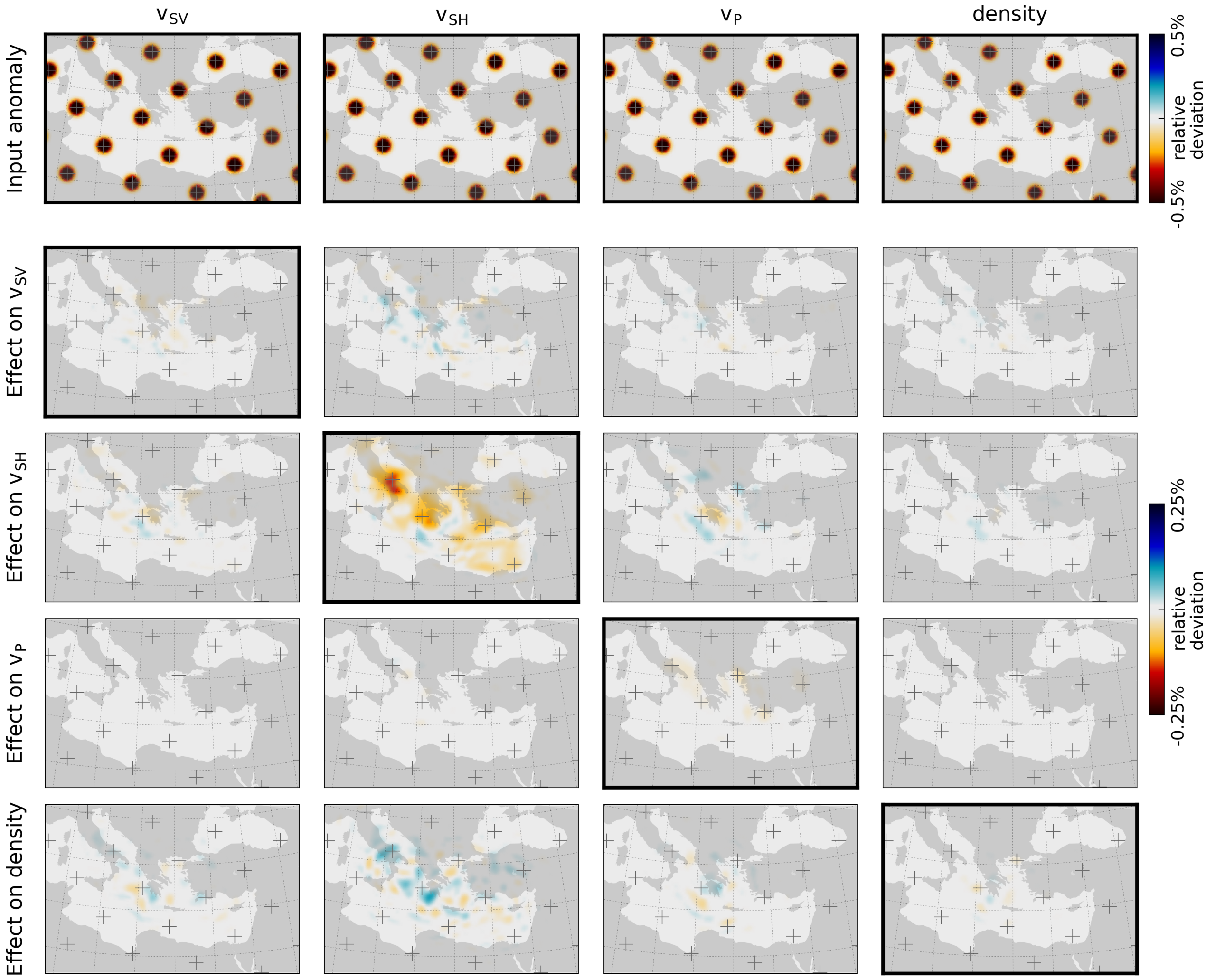

Figure S16: Spike tests conducted for model 91 in the period band 28–150 s, as described in Figure 15 of the paper. Results are here shown for a depth of 300 km.

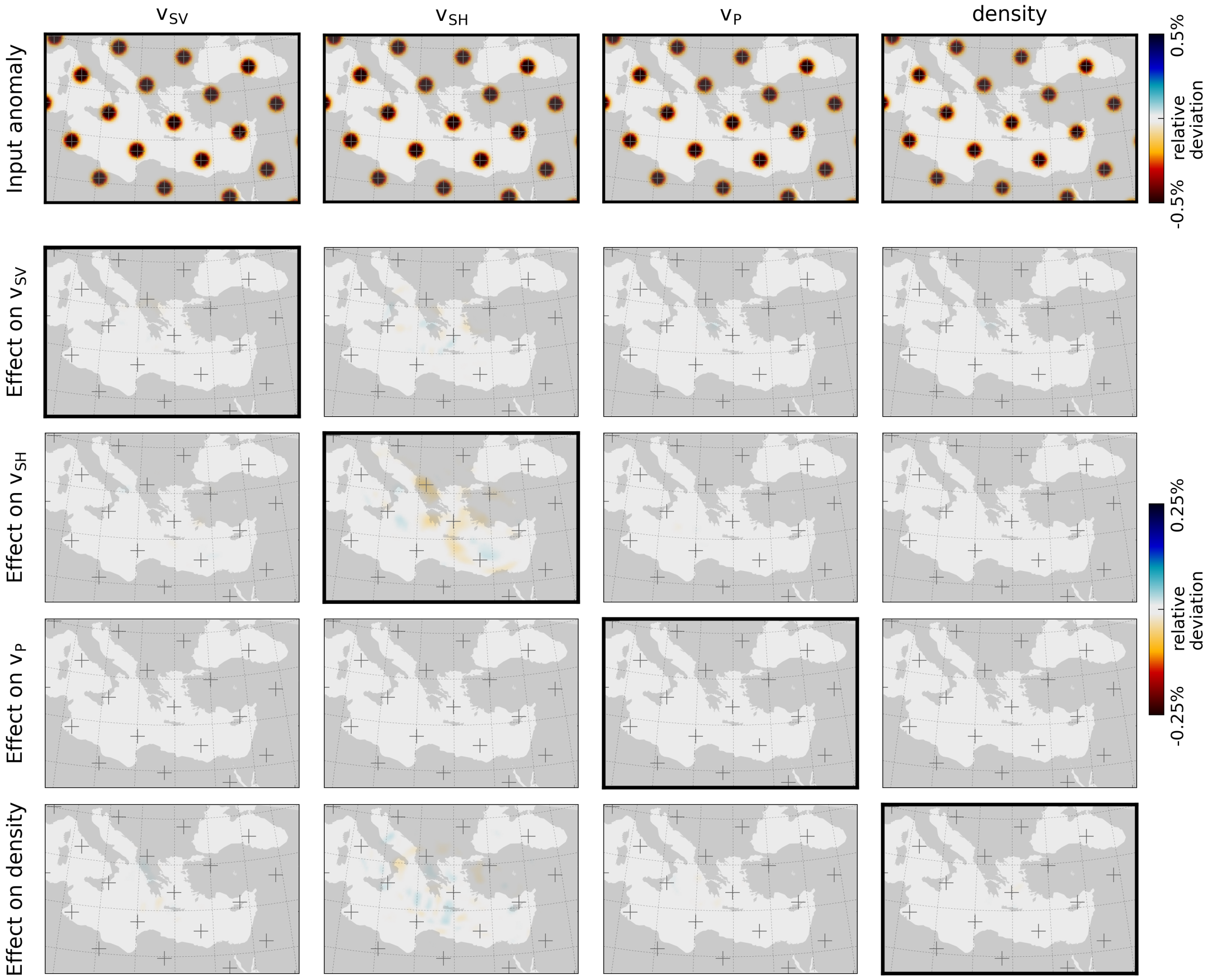

Figure S17: Spike tests conducted for model 91 in the period band 28–150 s, as described in Figure 15 of the paper. Results are here shown for a depth of 500 km.